A Fully Integrated Sensor-Brain-Machine Interface System for Restoring Somatosensation

Xilin Liu, *Member, IEEE,* Hongjie Zhu, *Member, IEEE,* Tian Qiu, Srihari Y. Sritharan, Dengteng Ge, Shu Yang, Milin Zhang, *Senior Member, IEEE,* Andrew G. Richardson, *Senior Member, IEEE,* Timothy H. Lucas, *Member, IEEE,* Nader Engheta, *Life Fellow, IEEE,* and Jan Van der Spiegel, *Life Fellow, IEEE*

***Abstract*— Sensory feedback is critical to the performance of neural prostheses that restore movement control after neurological injury. Recent advances in direct neural control of paralyzed arms present new requirements for miniaturized, low-power sensor systems. To address this challenge, we developed a fully-integrated wireless sensor-brain-machine interface (SBMI) system for communicating key somatosensory signals, fingertip forces and limb joint angles, to the brain. The system consists of a tactile force sensor, an electrogoniometer, and a neural interface. The tactile force sensor features a novel optical waveguide on CMOS design for sensing. The electrogoniometer integrates an ultra low-power digital signal processor (DSP) for real-time joint angle measurement. The neural interface enables bidirectional neural stimulation and recording. Innovative designs of sensors and sensing interfaces, analog-to-digital converters (ADC) and ultra wide-band (UWB) wireless transceivers have been developed. The prototypes have been fabricated in 180nm standard CMOS technology and tested on the bench and *in vivo*. The developed system provides a novel solution for providing somatosensory feedback to next-generation neural prostheses.**

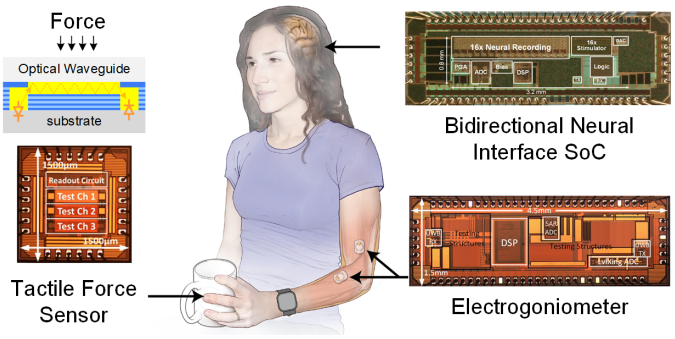

***Index Terms*— Force sensor, joint angle sensor, neural interface, neural prosthesis, system-on-chip**

I. Introduction

SOMATOSENSATION — the sense of touch and posture derived from mechanoreceptors in the skin, muscles, and joints — is especially important for dexterous control of hand and limb movements [1], [2]. Correspondingly, this sensory feedback is also important for prosthetic systems designed to replace hand and limb function following amputation or paralysis.

Neural prostheses can restore functional movements after injury by establishing a brain-machine interface (BMI). These systems decode movement-related information from neural recordings and transform it into control commands to drive a robotic arm [3]. In most BMI demonstrations, the sole feedback to the user is the visual correspondence between intended and actual movements. However, this does not yield adequate performance in many real-world tasks involving interaction forces with the environment (e.g. grasping and lifting a cup) [4]. Thus, robotic arms can be equipped with sensors that transduce somatosensory stimuli [5]. The sensor output can then be encoded into the brain through electrical stimulation at a point above the injury along the neural pathway that normally processes this information: peripheral nerves [6], [7], subcortical nuclei [8], [9], or somatosensory cortex [10], [11]. We refer to this as a sensor-brain-machine interface (SBMI).

For paralyzed individuals, the user experience of using robotic limbs is suboptimal [12]. The ideal rehabilitative strategy is to reanimate the person's own paralyzed limb. Recent work has demonstrated that this is possible using brain-controlled functional electrical stimulation of arm and hand muscles [13], [14]. However, the paralyzing injury also prevents the mechanoreceptor signals within the reanimated limb from reaching the brain. Artificial sensors of somatosensory stimuli are again needed to provide the feedback required for skillful movement. Due to the numerous differences from robotic arms, including the potential for actuator (muscle) fatigue and the restriction of device components such as wires, batteries, and sensors to surface (i.e. skin) layers, a new sensor strategy is required for reanimated arms.

This work was supported by National Science Foundation grant CBET-1404041.

Xilin Liu, Hongjie Zhu, Tian Qiu, Nader Engheta, and Jan Van der Spiegel are with the Department of Electrical and Systems Engineering, University of Pennsylvania, Philadelphia, PA, 19104 USA.

Milin Zhang is with the Department of Electronic Engineering, Tsinghua University, Beijing, China, 100084.

Srihari Y. Sritharan, Andrew G. Richardson, and Timothy H. Lucas are with the Department of Neurosurgery, University of Pennsylvania, Philadelphia, PA, 19104 USA.

Dengteng Ge is with the Institute of Functional Materials, Donghua University, Shanghai, China, 200336.

Shu Yang is with the Department of Materials Science and Engineering, University of Pennsylvania, Philadelphia, PA, 19104 USA.

In this work, we propose a novel sensor strategy for restoring somatosensation using a SBMI system, as illustrated in Fig. 1. In this new strategy, multiple wireless sensor nodes

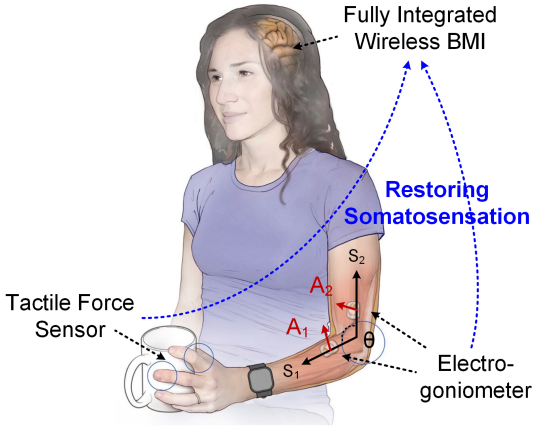

Fig. 1. Illustration of the proposed wireless sensor-brain-machine-interface (SBMI) system. The system links multiple body-area sensors (e.g. tactile force sensor, electrogoniometer, etc.) and an invasive BMI for continuous somatosensation restoration.

would be worn on or implanted under the patient's paralyzed limb and have a minimal physical presence, free from the constraints of gloves or wires. Ideally, the sensors would cause minimal additional loads on the muscles and joints and be nearly transparent to the user. A wireless BMI device with an invasive neural interface would provide sensory encoding by continuous electrical stimulation with the stimulus amplitude or frequency modulated by the sensors' outputs. This strategy could provide superior intuitive sensation restoration to paralyzed individuals, but places great demands on the specifications of the sensors and associated electronics, including power consumption and device dimension. To the best of our knowledge, none of the existing commercial medical devices or reported work in literature meet all requirements of this novel sensor strategy. In this work, we fill this important research gap by developing a custom SBMI system with innovative sensors, electronics and system integration. Below, we analyze the design considerations of each key building block.

A. Tactile Force Sensor

Human skin, and the fingertip in particular, provides high sensitivity to force across a range of frequencies [15]. Interest in miniature force sensors with high sensitivity has increased in recent years due to their potential applications in electronic skins, touch screens, and medical diagnostics [16], [17]. Microelectromechanical systems (MEMS) are one of the fastest-growing technologies in the miniaturized force sensor market [18]. However, MEMS sensors usually require specialized micro-fabrication processes [19], [20], which leads to a high cost. As an alternative, polymer-based optical force sensors have advantages including scalability and insensitivity to electronic noise. Elastomeric polydimethylsiloxane (PDMS) is typically used as a compressible optical cavity or waveguide. Optical pressure sensors consisting of optical fibers and PDMS waveguides have been demonstrated [21], [22]. Thanks to advancements in silicon light-emitting devices (Si-LED) [23], optical waveguides have become feasible to implement in standard CMOS technology. Using this technology, we develop a wearable optical force sensor with a wireless transmitter.

B. Electrogoniometer

Proprioception is the sense of the relative position and movement of the body, which is essential for guiding movements. An electrogoniometer is a device used to measure joint angles. It typically employs sensors with relatively high power consumption, such as potentiometers or strain gauges, and thus is not suitable for long-term everyday use [24], [25]. In this work, an electrogoniometer is designed with custom-designed ICs and ultra low-power 3-axis MEMS accelerometers, achieving a very low power consumption and a minimum device dimension. The joint angle is calculated by an on-chip digital signal processor (DSP) using the measurements from the two accelerometers.

C. Bidirectional Neural Interface

In the past decade, there has been significant progress in the development of bidirectional neural interfaces, which integrate both neural recorder and stimulator [26], [27]. Initial studies have demonstrated long-term recording and stimulation in freely behaving animals using off-the-shelf components [28]–[30]. Subsequently, the systems became more integrated to improve performance and enable new applications [31], [32]. A bidirectional BMI was developed in which neural recording and processing subsystems were integrated into a commercial neural stimulator [33], [34]. A system-on-chip (SoC) with 64 recording channels and dual stimulation channels was designed [35] as was a 32-channel modular bidirectional BMI with an embedded digital signal processor (DSP) for closed-loop operation [36]. Another group developed a battery-powered activity-dependent intracortical microstimulation SoC with on-chip action potential discrimination and spike-triggered stimulation [37]. Follow-up work added an on-chip stimulation artifact rejection feature [38]. High channel count designs were developed including a 128-channel fully differential neural recording and stimulation interface [39] and a 320-channel bidirectional interface chip [40]. Finally, bidirectional neural interfaces have been designed for specific clinical applications, including control of epileptic seizures and movement disorders [41], [42].

The bidirectional neural interface in the present work builds from prior devices developed by our group. We previously developed a battery-powered, modular system with wireless sensor nodes and a bidirectional neural interface using off-the-shelf components [43], [44]. We also developed a fully-integrated bidirectional neural interface SoC with on-chip closed-loop controller [45], [46]. Here, we extend the latter design to include an ultra-wide band (UWB) wireless link to the sensor nodes and custom on-chip processing to create a low-power, SBMI system that could provide somatosensory feedback for a neural prosthesis.

Phased research progress towards the system described in this paper has been presented previously [47], [48]. The contributions of the present paper include the characterization of the optical force sensor and the electrogoniometer, the algorithm and DSP design details underlying the proprioceptive sensing, the methodology and implementation of the system integration, as well as experiments and quantification of the full SBMI system specifications.

II. System Overview

The proposed SBMI is a preclinical system with which artificial sensory encoding strategies can be validated in appropriate animal models. In an experiment of finger force encoding, the force sensor detects the fingertip force and sends the readout wirelessly to the neural interface device to deliver modulated stimulation to the brain. Typically, stimulus pulse amplitude or pulse duration would be linearly modulated with the force readout to encode the sense of touch [49], [50]. Similarly, in an experiment of proprioception encoding, the electrogoniometer calculates the joint-angle and sends it wirelessly to the neural interface device for modulated stimulation. Encoding both tactile and proprioceptive stimuli simultaneously could be achieved through separate neural stimulation channels targeting distinct circuits normally responsive to each modality. The neural interface device is worn on the animal's head or back with wired connections to electrodes implanted chronically into target brain regions. Although the recording capabilities of the neural interface SoC are not strictly needed for sensory encoding, they could be used either for movement decoding in a bidirectional neural prosthesis or to monitor stimulus-evoked neural activity for closed-loop encoding strategies [52].

The block diagrams of the proposed SBMI system are shown in Fig. 2. The system consists of a wireless tactile force sensor, a wireless electrogoniometer, and a wireless bidirectional neural interface SoC. The tactile force sensor node consists of a sensor node and a wireless sensor interface IC. The sensor node integrates photodiodes, waveguide channels, and analog readout circuits. The wireless sensor interface IC integrates a programmable analog interface, a low-power asynchronous level-crossing analog-to-digital converter (LxADC), and a UWB transmitter. The two chips are connected on a printed circuit board (PCB).

The electrogoniometer consists of a primary and a secondary node, which are to be attached to two body parts to measure their relative position. Each node has a custom-designed IC and an off-the-shelf 3-axis MEMS accelerometer, which are connected on a PCB. Each node has an analog interface and an ADC to digitize the accelerometer's output. The secondary node integrates a UWB transmitter for transferring the data to the primary node. The primary node integrates a custom-designed DSP, a UWB receiver and a UWB transmitter. The UWB receiver retrieves the data from the secondary node, the DSP processes the joint angle, and the UWB transmitter sends the calculated joint angle to the neural interface SoC, or external data logging system.

The neural interface SoC integrates: i) a 16-channel low-noise neural recording front-end, ii) a 16-channel programmable electrical stimulator, iii) a 10-bit successive approximation register (SAR) ADC, iv) a UWB wireless transceiver, v) a digital controller for generating timing and control signals, and vi) peripheral modules for power and analog references [27], [43]. The neural stimulator is designed to deliver biphasic charge-balanced stimulation in current-mode. The stimulation current amplitude is programmable. There are two modes designed for stimulating using clinical macroelectrodes and high-impedance microelectrodes. In the high-current mode designed for macroelectrodes, the stimu-

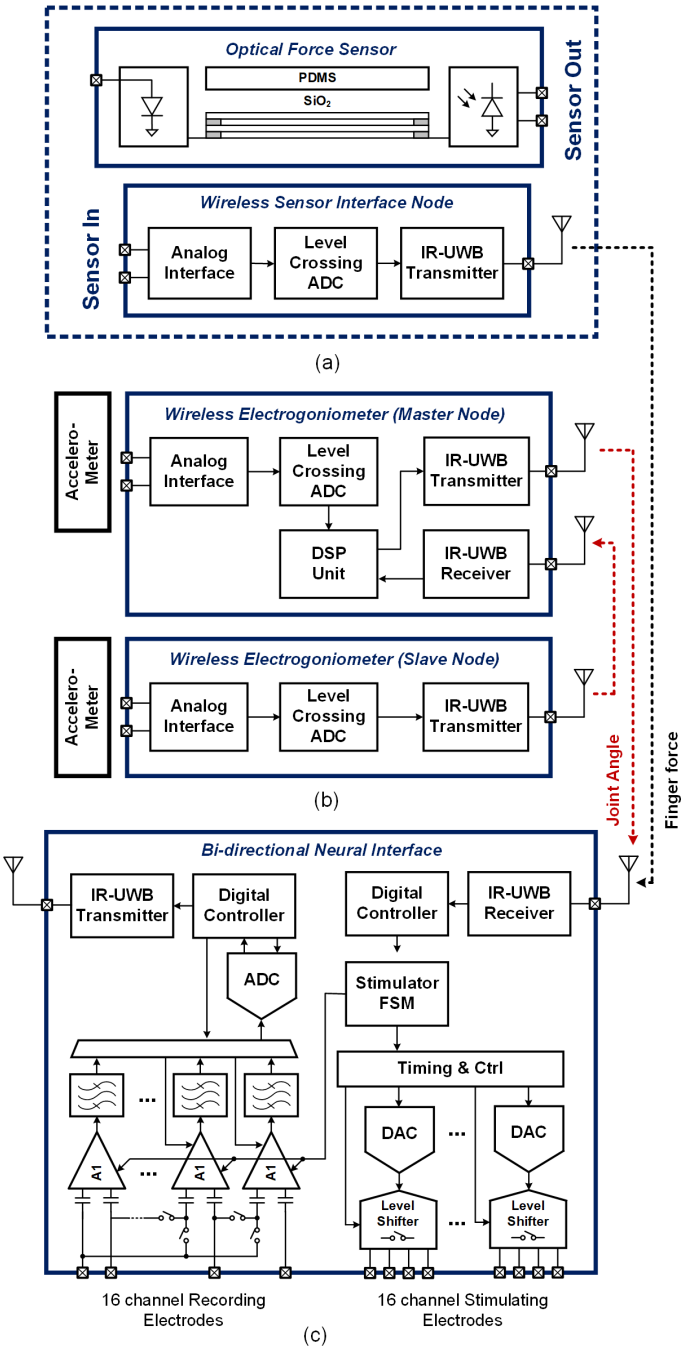

Fig. 2. Block diagrams of the proposed SBMI system. (a) The wireless optical force sensor, (b) The wireless electrogoniometer sensor pair, and (c) the bi-directional wireless neural interface SoC. Power management units are not shown.

lation current is programmable from 0 to 2mA; in the low-current mode designed for microelectrodes, the stimulation current is programmable from 0 to 200μA.

Local field potentials (LFPs) and action potentials (APs) are commonly used as control signals in sensorimotor BMI applications [51]. In this work, the neural recording front-end has been designed with two modes to record LFPs and APs. The LFP mode has a bandwidth of 0.3Hz-1kHz, with a low noise floor; the AP mode has a bandwidth of 100Hz-6kHz, with a relaxed noise floor. The ADC has been designed with a sufficient dynamic range (>45dB) and a sampling rate (>10kSps/channel) to capture the amplified neural signals.

III. Sensors and Circuits Design

A. Design of the Optical Tactile Force Sensor

Fig. 3 illustrates the optical force sensor design. A 600μm PDMS membrane is placed on top of the SiO_2 in standard CMOS die. The PDMS membrane is designed with an inverse-lenticular structured surface. As a result, the contact area between the PDMS and the SiO_2 is minimal when no force is applied, and the contact area increases with the applied force. During operation, a Si-LED emits light into the SiO_2 optical waveguide channel. A certain amount of light internally reflects and reaches the photodiode on the other side of the waveguide. The amount of the escaped light depends on the contact area of the PDMS and the SiO_2. Thus the readout of the photodiode changes monotonically with the applied force.

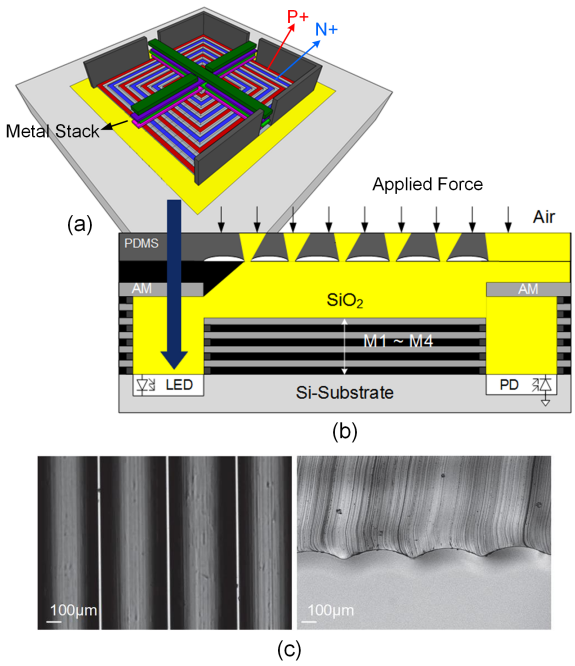

Fig. 3. Illustration of optical force sensor. (a) 3-dimensional view of the silicon LED, which uses interdigitated P+ N+ rings inside an N-well. (b) Side view of the optical force sensor (not to scale). (c) Micrographs of the top (left) and side (right) views of the fabricated PDMS membrane with an inverse-lenticular structured surface.

The PDMS material (SYLGARD 184, Dow Corning Co.) is composed of a 1:10 mixing ratio of the curing agent. The PDMS mixture is cast on a polystyrene lenticular lens board with a pitch of 20μm. After degassing for 30 minutes, the PDMS mixture and lenticular lenses molds are cured for 3 hours at 65°C. Finally, the PDMS membrane is carefully peeled off the mold. The PDMS membrane is cut into 800μm by 800μm pieces and placed on top of the CMOS chip with the inverse-lenticular strips perpendicular to the direction of the optical waveguide.

The Si-LED is designed using interdigitated P+ N+ rings inside an N-well. The size of the Si-LED is 80μm by 80μm. On the other side of the optical waveguide, a photodiode is designed using P+ and N-well with an active area of 80μm by 80μm. The readout circuit uses a 3-transistor active pixel structure. The optical waveguide channel has a size of 200μm by 600μm. The sidewalls of the Si-LED, the photodiode and the waveguide channel are shielded by stacked metal layers and vias for minimum light leakage. The bottom side of the optical waveguide channel is elevated to four metal layers, which effectively prevent the light from being absorbed by the silicon substrate. It also reduces the path length of totally internally reflected light traveling inside the channel by reducing the thickness of the SiO_2 layer in the channel, which effectively reduces the light loss in the SiO_2 medium.

B. Design of the Electrogoniometer

A dual-accelerometer system is used for measuring the joint angle of two rigid body segments, S_1 and S_2. The mounting of the two accelerometers are illustrated in Fig. 1.

Define $\widehat{n}_g$ as a unit normal vector of gravity. The measured accelerometer vector is defined as $\vec{A_1}$, $\vec{A_2} \in \mathbb{R}^3$, with respect to the local coordinate system. The cosine of the joint angle, θ, can be written as:

$$cos\theta = \frac{\vec{A_1} \cdot \vec{A_2}}{||\vec{A_1}||||\vec{A_2}||} \tag{1}$$

Here we define Γ_1 and Γ_2 as

$$\Gamma_1 = \left[\vec{A_1} \cdot \vec{A_2}\right]^2 \tag{2}$$

and

$$\Gamma_2 = \left[||\vec{A_1}||||\vec{A_2}||\right]^2 \tag{3}$$

The exact joint-angle θ can be solved based on the Eq. (1-3) as

$$\theta = cos^{-1}(\sqrt{\frac{\Gamma_1}{\Gamma_2}}) \tag{4}$$

However, the implementation of Eq. (4) significantly increases the complexity and power dissipation of the DSP hardware. In this work, we propose to use a simple linear equation to approximate the Eq. (4). The linear equation is given by

$$\theta' = \alpha(\frac{\Gamma_1}{\Gamma_2}) + \beta \tag{5}$$

where $\alpha = \beta = \pi/2$. The Eq. (4) and (5) are plotted in Fig. 4 for comparison.

Fig. 5 shows the block diagram of the hardware implementation. During the operation, the two 6-bit digitized vectors $\vec{A_1}$ and $\vec{A_2}$ are first sent into the DSP for computing three dot

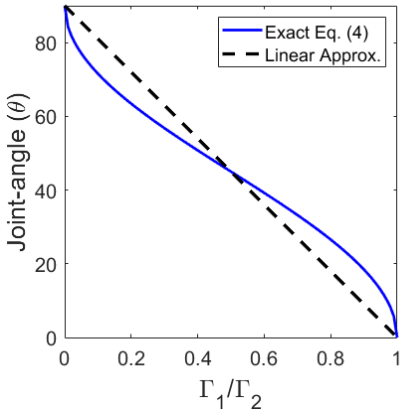

Fig. 4. Illustration of solving the joint-angle using the exact equation (Eq. 4) and the linear approximation (Eq. 5) implemented in this work.

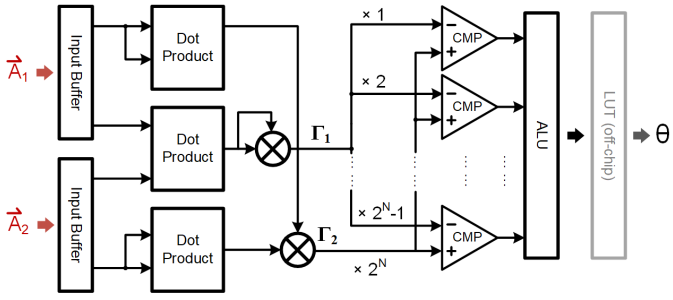

Fig. 5. Block diagram of the real-time joint angle calculation performed by the on-chip DSP. A linear N-bit approximation of θ is implemented on-chip, where N is 4. An off-chip look-up table (LUT) can be used to find the θ value.

products $(\vec{A_1} \cdot \vec{A_1})$, $(\vec{A_2} \cdot \vec{A_2})$, and $(\vec{A_1} \cdot \vec{A_2})$. The results are then used to produce Γ_1 and Γ_2.

To further reduce the computational cost, Γ_1/Γ_2 is quantized in 4-bit by a 16-level digital comparison instead of a full divider. Specifically, Γ_1 is amplified in parallel from $\times 1$ to $\times 15$, and Γ_2 is amplified by $\times 16$. The amplified versions of Γ_1 and Γ_2 are then compared in 15 individual digital comparators. At last, the comparators' output is fed into an arithmetic logic unit (ALU) for computing the linear equations Eq. (5). The final output is an estimated version of the joint-angle θ.

Since the function of Eq. (4) is monotonic, the θ value can also be calibrated off-chip using a look-up table (LUT). The accuracy of the proposed implementation is mainly limited by the quantization level. This is an intentional design choice because a 5.625° joint-angle resolution is sufficient for the sensory encoding purpose in this work.

C. Design of the Bidirectional Neural Interface

The neural interface SoC integrates 16 independent channels for bidirectional neural stimulation and recording. Fig. 6 (a) shows the circuit schematic of the stimulation driving site, which is shared between a group of four channels. The timing of each driving site can be individually programmed. The stimulator can perform both monopolar stimulation and bipolar stimulation. In the monopolar stimulation mode, one electrode is selected by a multiplexer; in the bipolar stimulation mode, two electrodes are selected from either the same or different driving sites [46]. Two 6-bit digital-to-analog converters (DACs) are designed to generate cathodic (sink) and anodic (source) stimulation currents. Each DAC consists of binary-weighted current sources, as shown in Fig. 6 (b). An additional 4-bit DAC is used for calibrating the static mismatches between the cathodic and anodic currents. The current of the sink DAC is intentionally reduced for a single-side calibration. A current comparator is integrated on-chip for calibration purposes. Regulating amplifiers are used to boost the output impedance.

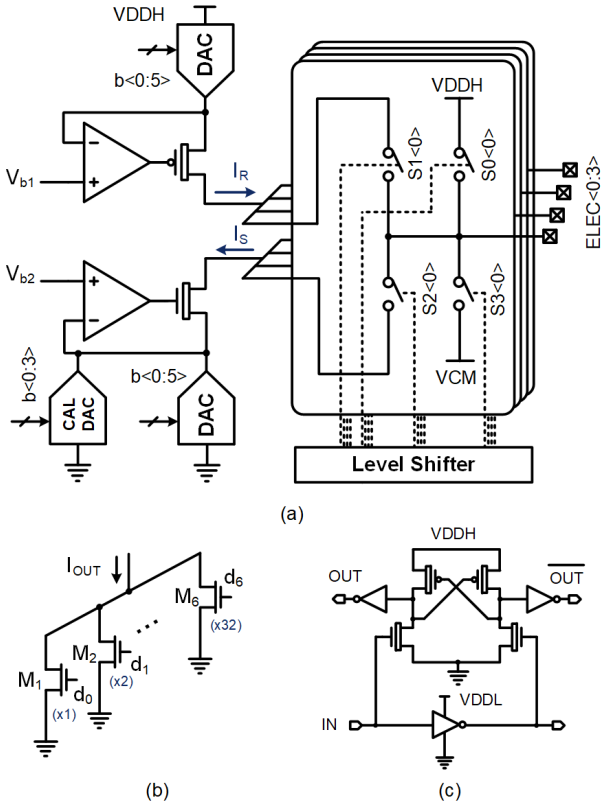

Fig. 6. Circuit diagrams of the neural stimulator. (a) the output stage with a 6-bit DAC and a 4-bit calibration DAC, (b) the binary weighted current DAC, and (c) the level shifter.

The stimulator has two modes: in the high-current mode, the output current range is 0-2048μA with a programmable step current of 32μA; in the low-current mode, the output current range is 0-255μA with a programmable step current of 4μA. Thick oxide devices are used to tolerate high stimulation voltage. Fig. 6 (c) shows the level shifters used to convert a low-voltage digital signal to a high-voltage switch control signal. The whole stimulator module can be gated to minimize power leakage.

The recording channel consists of a low-noise amplifier, a programmable transconductance-capacitance (Gm-C) band-pass filter, and a programmable gain amplifier (PGA). The key circuit diagrams of the low-noise neural recording front-end are shown in Fig. 7. The low-noise amplifier uses capacitive feedback to set the gain. The core operational transconductance amplifier (OTA) A1 uses a folded-cascode topology.

Chopping switches are integrated to remove the flicker noise [46], [53]. A capacitive positive feedback loop is used to boost the input impedance [55]. A DC servo loop is used to remove the DC offset. Chopping is disabled when configured to record APs.

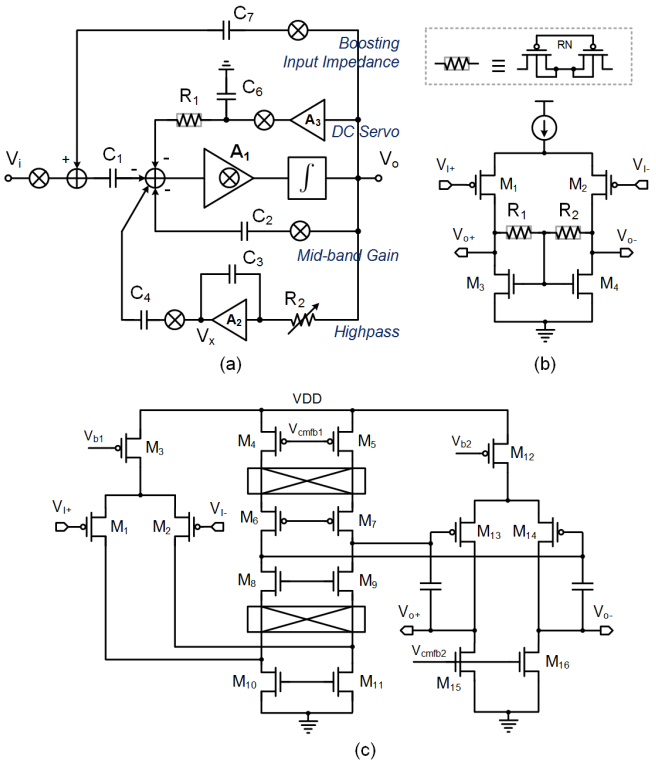

Fig. 7. Circuits schematics of the neural recording front-end, including (a) the capacitively-coupled chopping amplifier. Single-ended structure is used for illustration, (b) the fully-differential amplifier used in the highpass and DC-servo loop, and (c) the two-stage low-noise transconductance amplifier with chopping switches.

D. Design of the Analog-to-Digital Converters

Two ADCs have been designed in this work. First, a 10-bit SAR ADC is implemented in the neural interface SoC for the digitization of neural signals. Second, a 6-bit asynchronous LxADC is implemented in the sensor node for low-power sensor data digitization. SAR ADCs are suitable for low-power applications with moderate sampling rate requirements. In this work, a split capacitor array is used to reduce the area and power consumption. The capacitors are realized as a standard metal-insulator-metal (MIM) structure. A monotonic switching procedure is used to minimize the power consumption caused by unnecessary switching [45], [46], [53].

Asynchronous continuous sampling ADCs have been introduced in ultra-low power applications in recent years [56], [57]. LxADCs have a low output data rate and signal-dependent power consumption [56], [58], [59]. A 200nW ultra-low power event-driven ADC with limited bandwidth and dynamic range has been developed [60]. An adaptive resolution asynchronous ADC has been proposed to improve data rate, at the cost of circuit complexity [61]. Inspired by these designs, in this work, a low-power, high-speed asynchronous event-driven LxADC is developed for the sensor nodes. The block diagram of this LxADC is shown in Fig. 8 (a).

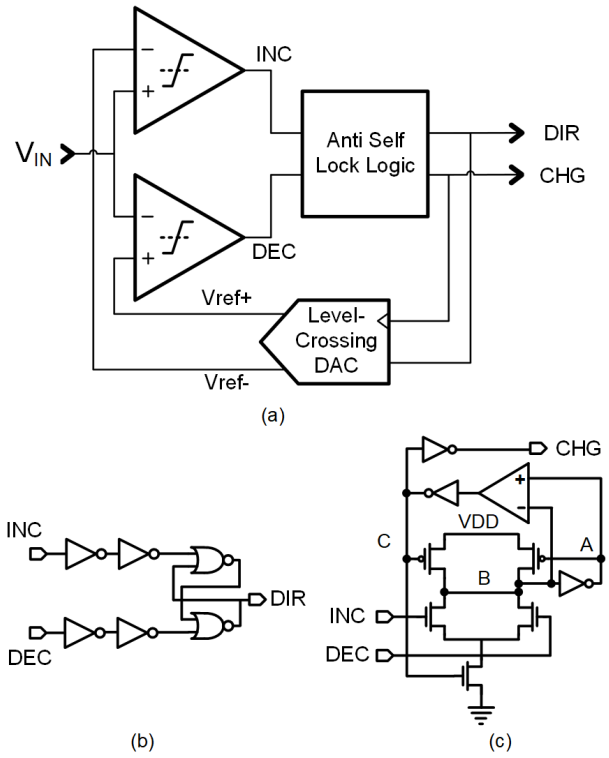

Fig. 8. (a) Block diagram for the proposed LxADC. Circuit schematics for the (b) “direction (DIR)” and (c) “change (CHG)” signal generation modules for anti-self-locking operation.

The LxADC tracks the changes of the input signal by comparing it with a set of hysteresis reference voltage levels using a pair of comparators [47]. After reset, the LxADC first catches up with the input signal at its maximum speed. Once it catches up with the input signal, the continuous-time sampling mode will start. A 64-level reference voltage generator is used to provide an effective resolution of 6-bit. The comparator pair generates an “increase (INC)” or a “decrease (DEC)” signal when the input voltage crosses the level of the upper or the lower reference voltage, respectively.

Self-locking is a critical issue in conventional LxADC designs. It occurs when the reference voltages, selected by the shift register, lose the capability for continuous tracking of the analog input voltage. Self-locking status often happens during 1) the circuit start-up phase, 2) circuit (shift register) reset phase, 3) conversion error, or 4) when the input signal changes faster than the circuit can respond. Fig. 9 illustrates the scenarios of self-locking without and with the proposed anti-self-locking circuit. When the LxADC enters the self-locking state, either the “INC” or the “DEC” signal stays high without a rising edge generated to drive the shift register. A LxADC can only get out of the self-lock status if the input signal goes back in between the selected upper and lower reference voltages.

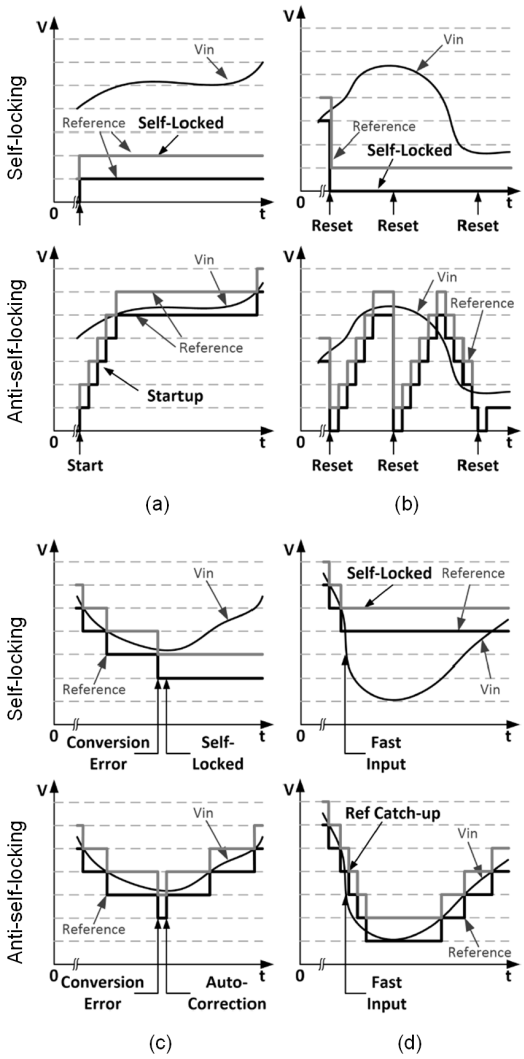

Fig. 9. Illustration of self-locking conditions of the LxADC (upper rows) and anti-self-locking behavior of the proposed design (lower rows). Typical scenarios including operations during (a) ADC startup, (b) asynchronous resets, (c) conversion error, and (d) when the input signal changing faster than the LxADC's bandwidth.

To release LxADCs from the self-locking state, anti-self-locking signals "direction (DIR)" and "change (CHG)" are generated, as shown in Fig. 8 (b) and (c), respectively. The "DIR" signal controls the direction of the shift register. In normal operations, the "CHG" generation module passes the rising edges of the "INC" or "DEC" signal to the "CHG" output. If the LxADC enters a self-locking state, the self-controlled delay loop formed by nodes B, A and C, generates rising edges of "CHG" signals to drive the shift registers to update the reference voltage selection, until the LxADC exits. The maximum response speed of the LxADC is determined by the delay of the self-controlled loop in the regenerative "CHG" signal generation circuit. In order to avoid overshooting conversion of the LxADC, the delay of the self-controlled delay loop is designed to be longer than the conversion time of the input signal comparators.

The comparator, which is biased with a 30nA current, will delay the change of the voltages at nodes A and B at its input to the change of its output node by 0.5μs. A "CHG" signal is associated with the output of the comparator. The delayed change at node C will evoke the recharge of node B and discharge of node A, and hence the output of the comparator will be delayed again by 0.5μs to make node C high. If either the "INC" or the "DEC" signal is high at the moment when node C is recharged, node B will be discharged again and the loop will then generate another pulse for the "CHG" signal. With the regenerative "CHG" signal generation circuit, the proposed LxADC will be immune to self-locking states. Hence, the proposed LxADC features better robustness and makes an asynchronous reset function possible.

E. Design of the Ultra-Wide Band Wireless Transceiver

Impulse-radio UWB transceivers are widely used in near-range, power-sensitive applications. They are especially suitable for short-range wireless biomedical systems [62]–[64], given the simple circuit structure, low power consumption, and high data rate. The block diagram of the UWB transceiver designed in this work is shown in Fig. 10.

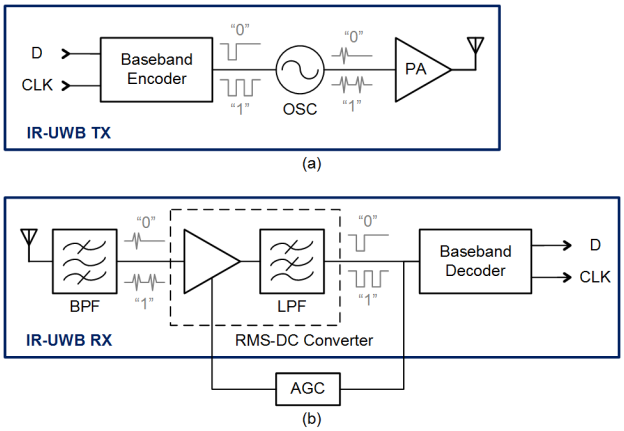

Fig. 10. Block diagram of the UWB (a) transmitter and (b) receiver.

The transmitter integrates a baseband generator, a RF pulse generator, and a power amplifier (PA). The baseband generator modulates digital input data into different numbers of short pulses. The pulse width is tunable under different data rates or transmission duty cycles. The RF pulse generator upconverts the short pulses to RF frequency. The oscillation frequency of the ring oscillator is tunable over a range of 100MHz. The RF pulse generator was implemented as a ring oscillator with a programmable number of stages.

In the receiver, the RF signal is first bandpass filtered at its corresponding operating frequency and then amplified by a low-noise amplifier. The output is fed into a RF power to root-mean-square voltage (RF-RMS) converter for downconversion. A comparator recovers the baseband short pulses, and a digital pattern recognition logic circuit demodulates the recovered signal to data and clock [47].

IV. Experimental Results

The designed prototype ICs have been designed in Cadence Virtuoso and fabricated in 180nm CMOS technology.

Microphotographs of the ICs are shown in Fig. 11, with major building blocks highlighted. The optical force sensor occupies 1mm×1mm, and the wireless sensor interface takes 1.1mm×0.4mm. The size of the wireless electrogoniometer is 4mm×1.1mm. The primary and secondary nodes are physically designed in the same silicon chip and specified through different configurations. The size of the neural interface SoC is 3.2mm×0.8mm.

The fabricated ICs and off-the-shelf electronics were assembled on PCBs. Autodesk EAGLE was used for designing the PCBs. The off-the-shelf components in the devices mainly consist of a general-purpose microcontroller (MCU), a power management unit, and a lithium battery. The MCU model used in this work is Atmel ATxmega128A1U. The MCU is used for configuring the custom ICs, and is put in the power-down mode after the initial configuration for minimizing the power dissipation. A 3.7V 40mAh lithium-ion polymer battery from Adafruit is used for powering the device. The weight of the assembled BMI device and sensor nodes is less than 5g. In addition to these devices, a wireless computer interfacing dongle has also been designed for communication and data logging. A graphic user interface has been designed using MATLAB from MathWorks. The system design reuses aspects of our previous work [43], [46].

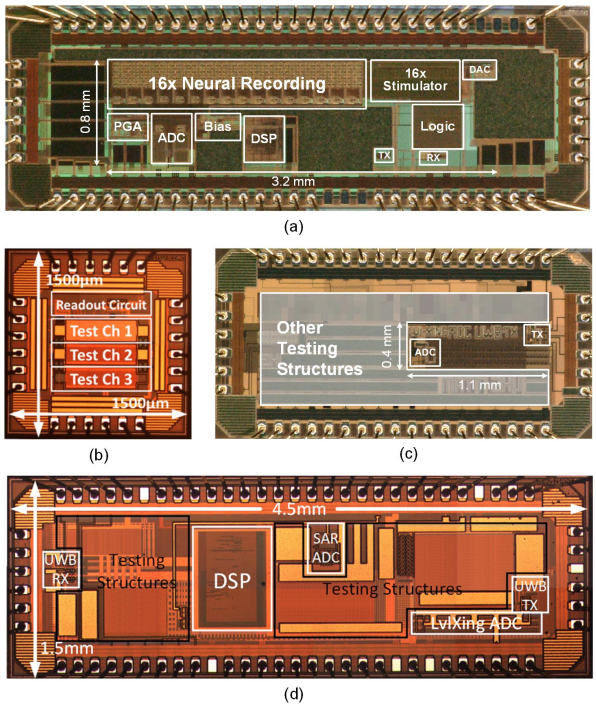

Fig. 11. Micrographs of fabricated ICs: (a) the bi-directional neural interface SoC, (b) the optical force sensor, (c) the sensor interface node, and (d) the electrogoniometer. Major building blocks are highlighted.

A. Bench Testing

The fabricated silicon photodiode was characterized with and without the PDMS membrane. The experimental result suggests that the optical waveguide makes a negligible impact on the amount of light received by the photodiode. An external force ranging from 0 to 0.87N was applied to the optical force sensor, and the sensor's outputs were measured. Fig. 12 shows the results of the measurement before calibration. The sensor response was monotonic with a nonlinearity of 2.53%. A linear regression exhibits a R^2 value of 0.9892. A LUT can be employed to further improve the linearity by calibration. The sensitivity of the sensor is 13.6mN, corresponding to 2.125kPa with an 800μm×800μm PDMS membrane area. Fig. 13 shows the measured outputs of the electrogoniometer with different input angles. The nonlinear output codes were corrected offline by using a LUT. The readout of the electrogoniometer gives a sufficient resolution for the sensory restoration requirement in this work.

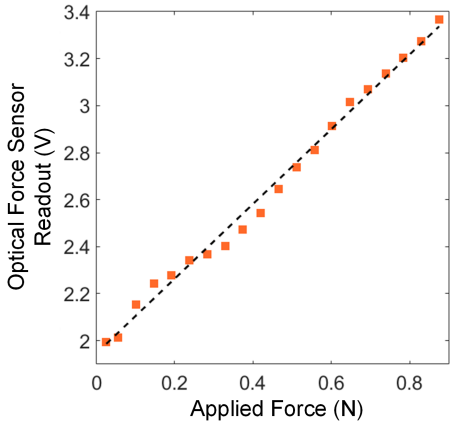

Fig. 12. Measured outputs of the designed optical force sensor with respect to applied force without calibration. The measurement shows a good linearity with a R^2 value of 0.9892 within the force range of interest.

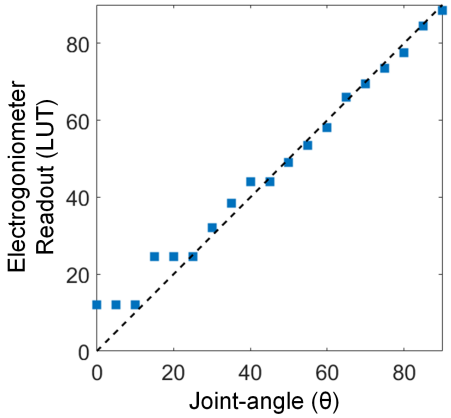

Fig. 13. Measured outputs of the designed electrogoniometer versus different input angle (θ). The output digital codes were corrected offline using a LUT.

The designed neural stimulator has been tested for static and dynamic performance. The static mismatch between the cathodic and anodic current was 1.9% before calibration, and 0.23% after calibration. The stimulator's output currents were measured with DC output voltage. Fig. 14 shows the measurement results in the low current mode with input codes

1, 4, 15, and 63. The compliance range of the stimulator output stage was 95% of the supply voltage. Dynamic testing was conducted using a passive load consisting of a 1nF capacitor and 1kΩ in series. After calibration, a continuous 100-pulse train was delivered to the load without charging. The residue charges were measured, and the charge error during one stimulation pulse was calculated to the 0.35% in this test.

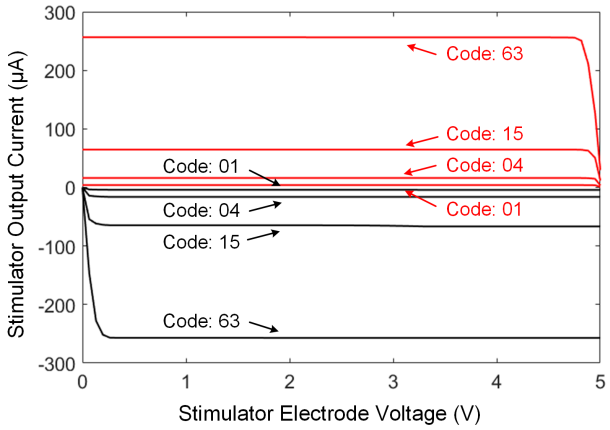

Fig. 14. Measured stimulator output currents versus the output voltage of the electrode in different input codes. The compliance range of the designed stimulator was 95% of the supply voltage.

The measured frequency responses of the low-noise amplifier in different bandwidth modes are shown in Fig. 15. The measured mid-band gain of the low-noise amplifier was 49.6 (34dB), and the common-mode rejection ratio (CMRR) was above 83dB in the worst case. The corner frequency of the low pass filter is programmable from about 200Hz to 6kHz. The measured input-referred noise of the low-noise amplifier in the 0.3Hz to 1kHz bandwidth is 1.58μV with chopping, which yields a noise efficiency factor (NEF) of 3.84 in LFP recording. The integral input-referred noise from 100Hz to 6kHz without chopping is 3.12μV, which yields a NEF of 2.82 in AP recording.

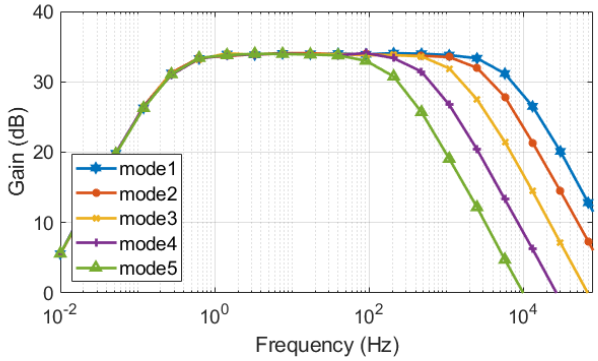

Fig. 15. Measured frequency responses of the low-noise amplifier in different bandwidth modes. The bandwidth modes were configured by programming the Gm-C filter.

The LxADC works under a wide range of supply between 0.8V and 2.0V. The input voltage range is from 0.2V to VDD-0.15V. The measured output of the LxADC was synchronously recorded with a 1MHz sampling clock for storing, plotting, and post-digital signal processing. The maximum input signal slew rate of the ADC is 0.026V/us. The power consumption of the ADC is 5μW at a 0.8V supply with a 1kHz sinusoidal input signal. The SNDR of the LxADC is 46.2dB with a 5kHz sinusoidal input. The figure-of-merit (FoM) is calculated as 13pJ/conv. The SAR ADC was measured with a sampling rate of 1MSps. The peak DNL and INL are -0.49/+0.56LSB and -0.82/+0.77LSB, respectively. The spurious-free dynamic range (SFDR) is 76.54dB and the signal to noise and distortion ratio (SNDR) is 56dB. The effective number of bit (ENOB) is 9.01 bit. The FoM is calculated as 43pJ/conv.

The impulse radio UWB transmitter and receiver can operate over a supply range. The transmitter works from 1.2V to 2V, while the receiver works from 0.8V to 2V. The continuous RF output power is -33dBm, which can be increased to -13dBm with the high power PA on. The sampling clock frequency is tunable between 10MHz to 160MHz. The maximum data rate is 10Mbps, the measured power consumption of the transmitter is 4.6pJ/bit, and the receiver's power consumption is 1.12nJ/bit.

B. In-vivo Testing

A subset of the functions of the SBMI system has also been tested *in-vivo*. All tests were approved by the University of Pennsylvania Institutional Animal Care and Use Committee. A high-density electrode array was implanted in the somatosensory brainstem of a rhesus macaque [65]. Electrogoniometer nodes were fixed with elastic bands to the chest and upper arm of the sedated macaque to measure the shoulder angle. The neural interface was configured to record APs from a brainstem neuron sensitive to shoulder movements. A clear correlation between the joint angle and the AP firing rate was observed during shoulder abduction (Fig. 16).

In addition, the bidirectional recording-stimulating capability of the neural interface was tested in an anesthetized Sprague-Dawley rat. A single stimulus pulse was repeatedly delivered to an electrode placed in the somatosensory cortex. The stimulus-evoked potential was recorded on a second electrode placed in the motor cortex. Fig. 17 shows an overlay of the evoked potentials from 10 trials aligned with the simulation time. The experiment has demonstrated that the SBMI is capable of reliably evoking neurophysiological responses from stimulation of somatosensory areas.

During the sensation restoration operation, each wireless sensor node can individually trigger a pre-defined stimulus in the neural interface device. The stimulation parameters and activating electrodes are selected by experts and preloaded to the MCU. Either intensity or frequency of the stimulation can be linearly modulated by the sensor's output in real-time. The overall latency, including the wireless link, from the sensor node to the neural interface device was measured to be less than 2.5μs. In practice, the updating frequency of the stimulation parameters is typically limited by the sampling rate of the sensors.

To summarize the experimental results, key measured specifications of our SBMI system are listed in Table I. The power

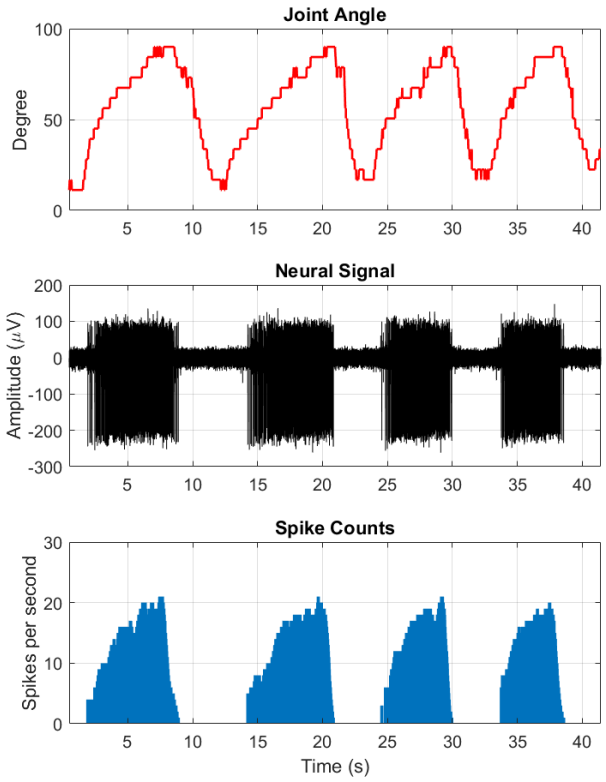

Fig. 16. *In-vivo* measurement of the electrogoniometer and the neural interface. (a) Measured joint angle, (b) recorded APs from a neuron, and (c) calculated spike rate of the APs using a moving window. A good correlation is shown between the joint-angle and AP firing rate.

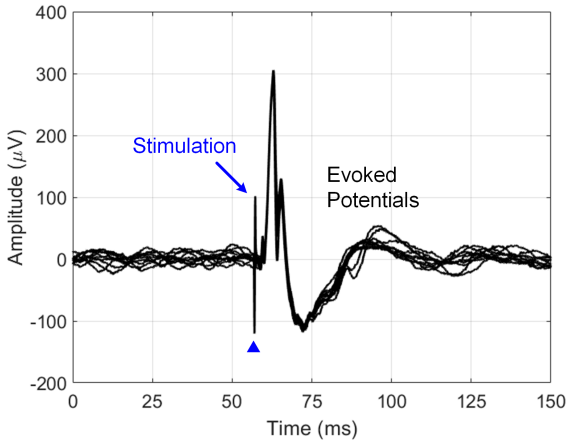

Fig. 17. *In-vivo* measurement of the bidirectional neural interface. Stimulation pulses were delivered to the somatosensory cortex of an anesthetized rat and the evoked potentials in the motor cortex were recorded. An overlay of 10 trials aligned with the stimulation time is shown in this figure.

dissipation numbers listed in the table have been measured in the continuous modulation mode. The battery life of the devices is more than 24 hours. Finally, Table II compares several key features of our system with recently reported BMI systems. Note that the noise performance in the LFP recording mode has been listed for comparison.

TABLE I
MEASURED SPECIFICATIONS SUMMARY

Module	Specs	Performance
Recording Front-end	LNA Gain	34dB
	LNA Noise	1.58μV (0.3-1kHz, w/ chopping)
		3.12μV (100-6kHz, w/o chopping)
	CMRR	>83dB
	AFE Power	8.3μW per ch
Neural Stimulator	Stim. Current	0 - 255μA/2mA
	Amplitude Res.	6-bit
	Pulse width	1μs - 250μs
	Stim. Frequency	0.5Hz - 300Hz
	Charge Error	0.35%
UWB Tranceiver	TX Output power	-33dBm
	TX/RX min supply	1.2V/0.8V
	Frequency	1.6 - 1.7GHz
	Max data rate	10Mbps
	UWB TX power	4.6pJ/bit
	UWB RX power	0.32nJ/bit
SAR/ LxADC	Sampling Rate	1M/5kHz
	ADC ENOB	9.0/6
	Power supply	1.8/0.8V
	LxADC power	13pJ/conv
Force Sensor	Sensitivity	13.6mN
	Non-linearity	2.53%
Power Consumption	BMI device	1.4mW
	Force Sensor	0.7mW
	Electrogoniometer	1.1mW (primary node)
		0.2mW (secondary node)

V. CONCLUSION

In this paper, a fully integrated wireless SBMI system has been presented. The system consists of a wireless bidirectional neural interface and custom-designed sensor nodes for transducing key somatosensory stimuli. A novel optical force sensor in standard CMOS with low-cost post-fabrication has been developed. Since the sensor is compatible with CMOS circuits, the sensor and all processing circuits can be integrated into a single chip in the future. The miniature design is compatible with tactile sensing on hands that have lost sensation due to injury. Key future issues to address are potential wireless sensor powering strategies and robustness of the design to repeated mechanical loading during daily use.

An electrogoniometer has been designed with custom circuits and low-cost accelerometers, which significantly reduces the power consumption compared with the strain gauges widely used in biomechanical studies. A custom-designed on-chip joint angle digital processor has been designed. The custom DSP minimizes the delay in joint angle calculation, which is critical in real-time sensory encoding paradigms. Again, future work could focus on the wireless power of these sensor nodes for a fully wireless SBMI. An asynchronous event-driven LxADC has been designed, which reduced the wireless data rate significantly compared with a conventional synchronous Nyquist-rate sampling system. The custom-designed impulse radio UWB wireless link achieves

TABLE II
COMPARISON WITH BIDIRECTIONAL BRAIN MACHINE INTERFACE DESIGNS

Reference	[42]	[36]	[43]	[35]	[46]	[66]	This work
Publication	2014 JSSC	2014 ESSCIRC	2015 TBioCAS	2015 JSSC	2016 TBioCAS	2016 TBioCAS	-
Technology	180nm	0.25μm/90nm	PCB	65nm	180nm	180nm	180nm
AFE ch #	4ch	32ch	3ch	64ch	16ch	4ch	16 ch
AFE Noise	6.3μVrms	100nV/rtHz	4.72μVrms	7.5μVrms	4.57μVrms	1.0μVrms	1.58μVrms
Bandwidth (Hz)	0.64-6kHz	100Hz	0.05-6kHz	10/1kHz-3k/8kHz	0.3-7kHz	0.25-250 Hz	0.3-1kHz (or 100-6kHz)
AFE NEF	3.76	Not reported	Not reported	3.6	4.77	2.5	3.84
Stim ch #	8ch Monopolar	16ch Monopolar	8ch Mono/ bipolar	8ch Bipolar	16ch Mono /bipolar	4ch	16ch Mono /bipolar
Stim Supply (V)	5V	Not reported	+/-12V	Not reported	Not reported	5V	5.5V
Max. Output (I)	4410μA	12mA	10mA	900μA	4mA	250μA	2mA
Sensors	-	-	Pressure Accelerometer Temperature	-	-	-	Pressure Accelerometer
ADC Mode	Pipeline log-ADC	$\Sigma\Delta$ ADC	12-bit SAR	10-bit SAR	SAR Current-mode	$\Sigma\Delta$ ADC	SAR/ LxADC
ADC ENOB	5.6	12	Not reported	8.2	9.1/7.9	9.4	9.0/6
ADC FoM	Not reported	Not reported	Not reported	Not reported	34.2fJ/conv-step 10.7fJ/conv-step	7.6 pJ/conv	43pJ/conv 13pJ/conv
On-chip proc	Custom DSP	Custom CPU	-	Custom DSP	Analog parallel	-	Custom DSP
Wireless Link	Custom backscattering	-	Commercial GFSK	-	Commercial Bluetooth	-	Custom UWB
Closed-loop	Yes	Yes	Yes	Yes	Yes	-	Yes
Application	Deep brain stimulation	Generalized	Generalized	Neuro-modulation	Generalized	Generalized	Sensory restoration

low power consumption in a small silicon area, which is especially suitable for short-range biomedical communication.

A bidirectional neural interface has been designed for neural stimulation and recording. The neural stimulator delivers biphasic charge-balanced stimulation with programmable current amplitude and frequency. The neural recorder amplifies LFP or AP signals with programmable gain and bandwidth. All of the ICs have been fabricated and evaluated in bench tests and *in vivo*. Compared with state-of-the-art designs summarized in Table II, this work demonstrates a novel integrated wireless system for sensation restoration, as well as novel circuit and sensor implementations. Based on the preliminary results, the proposed SBMI system provides a promising platform with which to test sensory encoding strategies in freely-behaving animal models and, in turn, advance next-generation, closed-loop neural prosthetics for individuals with paralysis.

REFERENCES

[1] A. G. Witney, *et al.*, "The cutaneous contribution to adaptive precision grip," *Trends Neurosci*, vol. 27, pp. 637-643, 2014.

[2] A. G. Richardson, M. A. Attiah, J. I. Berman, H. I. Chen, X. Liu, M. Zhang, J. Van der Spiegel, and T. H. Lucas, "The effects of acute cortical somatosensory deafferentation on grip force control," *Cortex*, vol. 74, pp. 1-8, 2016.

[3] L. R. Hochberg, *et al.*, "Reach and grasp by people with tetraplegia using a neurally controlled robotic arm," *Nature*, vol. 485, pp. 372-5, 2012.

[4] T. H. Lucas, *et al.*, "Strategies for autonomous sensor-brain interfaces for closed-loop sensory reanimation of paralyzed limbs," *Clin. Neurosurg.*, vol. 64, no. 1, pp. 11-20, 2017.

[5] N. Wettels, V. J. Santos, R. S. Johansson, and G. E. Loeb, "Biomimetic tactile sensor array," *Adv. Robotics*, vol. 22, pp. 829-49, 2008.

[6] D. W. Tan, *et al.*, "A neural interface provides long-term stable natural touch perception," *Sci. Transl. Med.*, vol. 6, pp. 257ra138, 2014.

[7] S. Raspopovic, *et al.*, "Restoring natural sensory feedback in real-time bidirectional hand prostheses," *Sci. Transl. Med.*, vol. 6, pp. 222ra19, 2014.

[8] S. Y. Sritharan, *et al.*, "Somatosensory encoding with cuneate nucleus microstimulation: detection of artificial stimuli," *Conf. Proc. IEEE Eng. Med. Biol. Soc.*, pp. 4719-22, 2016.

[9] A. J. Loutit and J. R. Potas, "Restoring somatosensation: advantages and current limitations of targeting the brainstem dorsal column nuclei complex," *Front. Neurosci.*, vol. 14, pp. e156, 2020.

[10] S. N. Flesher, *et al.*, "Intracortical microstimulation of human somatosensory cortex," *Sci. Transl. Med.*, vol. 8, pp. 361ra141, 2016.

[11] M. Armenta Salas, *et al.*, "Proprioceptive and cutaneous sensations in humans elicited by intracortical microstimulation," *Elife*, vol. 7, pp. e32904, 2018.

[12] C. H. Blabe, *et al.*, "Assessment of brain-machine interfaces from the perspective of people with paralysis," *J. Neural Eng.*, vol. 12, pp. 043002, 2015.

[13] C. E. Bouton *et al.*, "Restoring cortical control of functional movement in a human with quadriplegia," *Nature*, vol. 533, pp. 247-50, 2016.

[14] A. B. Ajiboye *et al.*, "Restoration of reaching and grasping movements through brain-controlled muscle stimulation in a person with tetraplegia: a proof-of-concept demonstration," *Lancet*, vol. 389, pp. 1821-30, 2017.

[15] R. S. Johansson and J. R. Flanagan. "Coding and use of tactile signals from the fingertips in object manipulation tasks," *Nat. Rev. Neurosci.*, vol. 10, pp. 345-59, 2009.

[16] T. Sekitani *et al.*, "A rubberlike stretchable active matrix using elastic conductors," *Science*, vol. 321, pp. 1468-1472, 2008.

[17] A. Chortos, J. Liu, Z. Bao, "Pursuing prosthetic electronic skin," *Nat. Mater.* vol. 15, pp. 937-50, 2016.

[18] D. Lopez, R. Decca, E. Fischbach, and D. E. Krause, "MEMS-based force sensor: Design and applications," *Bell Labs Technical Journal*, vol. 10, no. 3, pp. 61-80, 2005.

[19] S. Zhao, D. Parks, and C. Liu, "Design and modeling of a wide dynamic range hardness sensor for biological tissue assessment", *IEEE Sensors Journal*, vol. 13, no. 12, pp. 4613-4620, 2013.

[20] S. Sokhanvar, M. Packirisamy, and J. Dargahi, "MEMS endoscopic tactile sensor: Toward in-situ and in-vivo tissue softness characterization", *IEEE Sensors Journal*, vol. 9, no. 12, pp. 1679-1687, 2009.

[21] M. Ramuz *et al.*, "Transparent, optical, presure-sensitive artificial skin for large-area stretchable electronics," *Adv Mater.*, vol. 24, pp. 3223-3227, 2012.

[22] J. Missinne *et al.*, "High density optical pressure sensor foil based on arrays of crossing flexible waveguides," *Proc. SPIE 7716, Micro-Optics*, pp. 77161G, 2010.

[23] L. Snyman, M. du Plessis, and E. Bellotti, "Photonic transitions (1.4eV - 2.8eV) in silicon p+np+ injection-avalanche CMOS LEDs as function

of depletion layer profiling and defect engineering," *IEEE J. Quantum Electron.*, vol. 46, no. 6, pp. 906-919, 2010.

[24] J. Favre, B. Jolles, R. Aissaoui, and K. Aminian, "Ambulatory measurement of 3D knee joint angle." *J. Biomech.*, vol. 41, no. 5, pp. 1029-35, 2008.

[25] E. Palermo, S. Rossi, F. Marini, F. Patane, and P. Cappa, "Experimental evaluation of accuracy and repeatability of a novel body-to-sensor calibration procedure for inertial sensor-based gait analysis," *Measurement*, vol. 52, pp. 145-155, 2014.

[26] M. Zhang, Z. Tang, X. Liu and J. Van der Spiegel, "Electronic Neural Interfaces," *Nature Electroncis*, April 2020.

[27] J. Van der Spiegel, M. Zhang, and X. Liu, "System-on-a-Chip Brain-Machine-Interface Design - a Review and Perspective," *IEEE Int. Conf. Solid-State and Integrated Circuit Tech. (ICSICT)*, 2016.

[28] J. Mavoori *et al.*, "An autonomous implantable computer for neural recording and stimulation in unrestrained primates." *J. Neurosci. Meth.*, vol. 148, no. 1, pp. 71-77, 2005.

[29] S. Venkatraman, K. Elkabany, J. D. Long, Y. Yao, and J. M. Carmena, "A system for neural recording and closed-loop intracortical microstimulation in awake rodents." *IEEE Trans. Biomed. Eng.*, vol. 56, no. 1, pp. 15-22, 2009.

[30] S. Zanos, A. G. Richardson, L. Shupe, F. P. Miles, and E. E. Fetz, "The Neurochip-2: an autonomous head-fixed computer for recording and stimulating in freely behaving monkeys," *IEEE Trans. Neural Syst. Rehabil. Eng.*, vol. 19, no. 4, pp. 427-35, 2011.

[31] A. E. Mendrela *et al.*, "A bidirectional neural interface circuit with active stimulation artifact cancellation and cross-channel common-mode noise suppression." *IEEE J. Solid-State Circuits*, vol. 51, no. 4, 2016.

[32] A. Abdi and H. K. Cha, "A bidirectional neural interface CMOS analog front-end IC with embedded isolation switch for implantable devices," *Microelectronics J.*, vol. 58, pp. 70-75, 2016.

[33] A. G. Rouse *et al.*, "A chronic generalized bi-directional brain-machine interface," *J. Neural Eng.*, vol. 8, no. 3. pp. 036018, 2011.

[34] S. Stanslaski *et al.*, "Design and validation of a fully implantable, chronic, closed-loop neuromodulation device with concurrent sensing and stimulation," *IEEE Trans. Neural Syst. Rehabil. Eng.*, vol. 20, no. 4, pp. 410-21, 2012.

[35] W. Biederman *et al.*, "A 4.78mm2 fully-integrated neuro-modulation soc combining 64 acquisition channels with digital compression and simultaneous dual stimulation," *IEEE J. Solid-State Circuits*, vol. 50, no. 4, pp. 1038-1047, 2015.

[36] P. Cong *et al*, "A 32-channel modular bi-directional neural interface system with embedded DSP for closed-loop operation," *Eur. Solid-State Circuit Conf.*, 2014.

[37] M. Azin, D.J. Guggenmos, S. Barbay, R.J. Nudo, and P. Mohseni, "A battery-powered activity-dependent intracortical microstimulation IC for brain-machine-brain interface," *IEEE J. Solid-State Circuits*, vol. 46, no. 4, 2011.

[38] K. Limnuson *et al.*, "A bidirectional neural interface soc with an integrated spike recorder, microstimulator, and low-power processor for real-time stimulus artifact rejection," *IEEE Custom Integrated Circuits Conference (CICC)*, 2014.

[39] F. Shahrokhi and K. Abdelhalim. "The 128-channel fully differential digital integrated neural recording and stimulation interface," *IEEE Trans. Biomed. Circuits Syst.*, vol. 4, no. 3, 2010.

[40] R. Shulyzki *et al.*, "320-channel active probe for high-resolution neuromonitoring and responsive neurostimulation," *IEEE Trans. Biomed. Circuits Syst.*, vol. 9, no. 1, pp. 34-49, 2015.

[41] W. Chen *et al.*, "A fully integrated 8-channel closed-loop neural-prosthetic CMOS SoC for real-time epileptic seizure control," *IEEE J. Solid-State Circuits*, vol. 49, no. 1, pp. 232-247, 2014.

[42] H. Rhew *et al.*, "A fully self-contained logarithmic closed-loop deep brain stimulation SoC with wireless telemetry and wireless power management," *IEEE J. Solid-State Circuits*, vol. 49, pp. 2213-2227, 2014.

[43] X. Liu, M. Zhang, B. Subei, A. G. Richardson, T. H. Lucas, and J. Van Der Spiegel, "The PennBMBI: design of a general purpose wireless brain-machine-brain interface system," *IEEE Trans. Biomed. Circuits Syst.*, vol. 9, no. 2, pp. 248-258, 2015.

[44] X. Liu, B. Subei, Z. Milin, A. G. Richardson, T. H. Lucas, and J. Van der Spiegel, "The PennBMBI: A general purpose wireless Brain-Machine-Brain Interface system for unrestrained animals," *IEEE Int. Symp. Circuits Syst. (ISCAS)*, pp. 650-653, 2014.

[45] X. Liu, M. Zhang, A. G. Richardson, T. H. Lucas, and J. Van Der Spiegel, "A 12-channel bidirectional neural interface chip with integrated channel-level feature extraction and PID controller for closed-loop operation," *IEEE Biomed. Circuits Syst. Conf. (BioCAS)*, 2015.

[46] X. Liu, M. Zhang, A. G. Richardson, T. H. Lucas, and J. Van Der Spiegel, "Design of a closed-loop, bidirectional brain machine interface system with energy efficient neural feature extraction and PID control," *IEEE Trans. Biomed. Circuits Syst.*, vol. 11, pp. 729-742, 2016.

[47] H. Zhu *et al.*, "Design of a low power impulse-radio ultra-wide band wireless electrogoniometer," *IEEE Int. Symp. Circuits Syst. (ISCAS)*, pp. 770-773, 2015.

[48] X. Liu *et al.*, "A fully integrated wireless sensor-brain interface system to restore finger sensation," *IEEE Int. Symp. Circuits Syst. (ISCAS)*, 2017.

[49] F. M. Petrini *et al.*, "Sensory feedback restoration in leg amputees improves walking speed, metabolic cost and phantom pain," *Nat. Med.*, vol. 25, pp. 1356-63, 2019.

[50] H. Charkhkar, B. P. Christie, and R. J. Triolo, "Sensory neuroprosthesis improves postural stability during Sensory Organization Test in lower-limb amputees," *Sci. Rep.*, vol. 10, pp. 6984, 2020.

[51] R. A. Andersen, S. Musallam, B. Pesaran, "Selecting the signals for a brain-machine interface," *Curr. Opin. Neurobiol.*, vol. 14, pp. 720-6, 2004.

[52] J. Liu, H. K. Khalil, K. G. Oweiss, "Neural feedback for instantaneous spatiotemporal modulation of afferent pathways in bi-directional brain-machine interfaces," *IEEE Trans. Neural Syst. Rehabil. Eng.* vol. 19, pp. 521-33, 2011.

[53] X. Liu, *et al*, "A fully integrated wireless compressed sensing neural signal acquisition system for chronic recording and brain machine interface," *IEEE Trans. Biomed. Circuits Syst.*, vol. 10, pp. 874-83, 2016.

[54] X. Liu, *et al.*, "Design of a low-noise, high power efficiency neural recording front-end with an integrated real-time compressed sensing unit," *IEEE Int. Symp. Circuits and Syst. (ISCAS)*, pp. 2996-9, 2015.

[55] Q. Fan, *et al.*, "A 1.8 uW 60 nV/rtHz Capacitively-Coupled Chopper Instrumentation Amplifier in 65 nm CMOS for Wireless Sensor Nodes." *IEEE J. Solid-State Circuits*, vol. 46, no. 7, pp. 1534-1543, 2011.

[56] Y. Tsividis, "Event-driven, continuous-time ADCs and DSPs for adapting power dissipation to signal activity." *IEEE Int. Symp. Circuits Syst. (ISCAS)*, 2010.

[57] W. Tang *et al.*, "Continuous time level crossing sampling ADC for bio-potential recording systems," *IEEE Trans. Circuits Syst. I: Regular Papers*, vol. 60, no. 6, pp. 1407-1418, 2013.

[58] B. Schell and Y. Tsividis, "A continuous-time ADC/DSP/DAC system with no clock and with activity-dependent power dissipation," *IEEE J. Solid-State Circuits*, vol. 43, no. 11, pp. 2472-2481, 2008.

[59] C. Weltin-Wu and Y. Tsividis, "An event-driven clockless level-crossing ADC with signal-dependent adaptive resolution," *IEEE J. Solid-State Circuits*, vol. 48, no. 9, pp. 2180-2190, 2013.

[60] X. Zhang and Y. Lian, "A 300-mV 220-nW event-driven ADC with real-time QRS detection for wearable ECG sensors," *IEEE Trans. Biomed. Circuits Syst.*, vol. 8, no. 6, pp. 834-843, 2013.

[61] M. Trakimas and S. Sonkusale, "An adaptive resolution asynchronous ADC architecture for data compression in energy constrained sensing applications," *IEEE Trans. Circuits Syst. I: Regular Papers*, vol. 58, no. 5, pp. 921-934, 2011.

[62] R. K. Dokania, X. Y. Wang, S. G. Tallur, and A. B. Apsel, "A low power impluse radio design for body-area networks," *IEEE Trans. Circuits Syst. I: Regular Paper*, vol. 58, no. 7, pp. 1458-1469, 2011.

[63] Z. Zhang, Y. Li, K. Mouthaan, and Y. Lian, "A miniature mode reconfigurable inductorless IR-UWB transmitter-receiver for wireless short-range communication and vital-sign sensing," *IEEE J. Emerg. Sel. Topics Circuits Syst.*, vol. 8, no. 2, pp. 294-305, 2018.

[64] B. Benamrouche, A. Rumeau, and D. Dragomirescu, "Ultra-low power IR-UWB transceiver for wireless sensors network," *Int. Semiconductor Conf. (CAS)*, pp. 285-288, 2017.

[65] A. G. Richardson, P. K. Weigand, S. Y. Sritharan, T. H. Lucas, "A chronic neural interface to the macaque dorsal column nuclei," *J. Neurophysiol.*, vol. 115, no. 5, pp. 2255-64, 2016.

[66] E. Greenwald, *et al.*, "A Bidirectional Neural Interface IC With Chopper Stabilized BioADC Array and Charge Balanced Stimulator," *IEEE Trans. Biomed. Circuits Syst.*, vol. 10, no. 5, pp. 990-1002, 2016.